International Journal of Hydrogen Energy 87 (2024) 457–468

Contents lists available at ScienceDirect

International Journal of Hydrogen Energy

journal homepage: www.elsevier.com/locate/he

Closed-form analytical model for the cylinder region of thick-walled composite pressure vessels for hydrogen storage

Marie Hondekyn *, Nazim Ali, Wim Van Paepegem

Mechanics of Materials and Structures, Ghent University, Technologiepark-Zwijnaarde 46, 9052, Zwijnaarde, Belgium

ARTICLE INFO

Handling Editor: Prof. J. W. Sheffield

Keywords:
Hydrogen storage
Type IV pressure vessel
Fiber-reinforced composite
Closed-form analytical model
Design optimization

ABSTRACT

The rising interest in using hydrogen as a fuel has increased the demand for composite pressure vessels that can safely store hydrogen at a working pressure of 70 MPa. However, a significant challenge to commercialization lies in developing optimized vessel designs that minimize both cost and weight. Analytical models have proven valuable for design optimization since they enable a quick analysis of a large number of options. Despite this, existing models fail to combine three aspects that are essential for a correct analysis of hydrogen pressure vessels: validity for asymmetric lay-ups, including out-of-plane stresses since these are thick-walled vessels, and predicting stress variations near the dome-cylinder interface. Therefore, this work presents a closed-form analytical model that integrates these three features through a superposition of two models. The model's accuracy is evaluated by comparing the results with finite element simulations, showing excellent agreement across the entire stress distribution.

1. Introduction

In the global evolution towards net zero emissions by 2050, hydrogen is emerging as a promising energy vector for renewable energy to facilitate the decarbonization of the transportation sector. In this sector, hydrogen is particularly appealing to power heavy-duty vehicles that require high power outputs and long driving ranges, thanks to its high gravimetric energy density and fast refueling times [1–5]. However, its low volumetric energy density at atmospheric pressure necessitates storage at a high working pressure of 70 MPa to meet the desired driving ranges [5–7]. When storing compressed hydrogen gas at such high pressure levels, ensuring a safe and reliable pressure vessel design is crucial. This is typically achieved with Type IV pressure vessels, as these are high-strength, lightweight vessels with a high fatigue resistance and low risk for corrosion and hydrogen embrittlement [2,7,8]. A Type IV design comprises an inner polymer liner that acts as a barrier against hydrogen permeation, while a thick composite overwrap serves as the load-bearing component. A cylinder region and two domes can be distinguished, with metal bosses at the endcaps for refueling operations (Fig. 1). The composite overwrap is typically produced by filament winding, during which epoxy-impregnated carbon tows are wound at different angles α [2,8,9]. An optimal design of the composite overwrap features a well-balanced wrapping of hoop layers with fiber angles close to 90°, and helical layers with fiber angles smaller than 90°, to bear the load in both the hoop and axial direction of the vessel [6,9].

A challenge to commercialization of these pressure vessels lies in the extensive use of carbon fiber required to withstand the high loads, accounting for up to 70% of the total cost [2,8–11]. In this context, design optimization can enhance their economic viability by minimizing the use of carbon fiber, thereby reducing weight and cost and increasing the inner volume [2,11].

Different analysis methods can be used for the design optimization of Type IV vessels. Possible approaches are finite element (FE) simulations, such as by Ramirez et al. [8], Magneville et al. [10], and Leh et al. [12], and experimental testing. However, these methods are too time-consuming and expensive for the purpose of design optimization, as this involves a parametric variation of a large number of design variables [11,13]. One could think of analytical models instead, as these allow a quick calculation of many different designs, especially when implemented in an efficient coding environment. Moreover, an analytical approach offers more transparency and versatility compared to FE simulations, since every calculation step can be retraced and intermediate results can be obtained [11]. However, the key disadvantage of analytical models is that accuracy is often sacrificed by making simplified assumptions. A typical example is netting theory, which is a popular analytical tool for the preliminary design of pressure vessels that

* Corresponding author.
E-mail address: Marie.Hondekyn@UGent.be (M. Hondekyn).

https://doi.org/10.1016/j.ijhydene.2024.08.447
Received 12 July 2024; Received in revised form 26 August 2024; Accepted 27 August 2024
Available online 9 September 2024

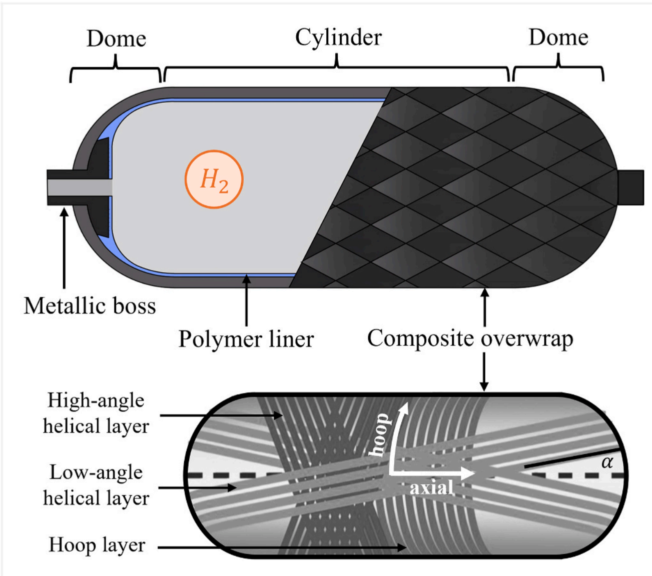

Fig. 1. Composition of a Type IV composite pressure vessel.

calculates the required thickness of the hoop and helical layers using two simple formulas. However, it is based on the unrealistic assumption that only fibers carry the load and are tensioned equally, neglecting any fiber interaction or resin contribution. Moreover, it can handle only one type of hoop and helical layer [2,6,7,9,13–15]. Because of these limitations, many researchers have focused on developing more reliable analytical models for the mechanical behavior of composite pressure vessels. Note that since pressure vessels are typically designed to have safe burst failure occurring in the cylinder region [8,12], many of these analytical methods address the cylinder region only. Generally, more advanced analytical models fall into two categories: those based on Classical Laminate Theory (CLT) and those based on 3D elasticity theory.

Classical Laminate Theory was used by Madhavi et al. [15], Alcantar et al. [16] and Camilleri et al. [17] to predict the membrane effects of laminated cylinders under pressure. However, it was emphasized by Jiang et al. [11], Park and Kim [13], and Belardi et al. [18] that in addition to the membrane loads, bending loads should be included as well due to the connection of the cylinder region to the dome. Their work demonstrates that additional stresses occur in the dome-cylinder transition region, and that these can be addressed analytically by a local bending moment M_x^0 and shear force Q_x^0 at the junction. Nevertheless, the aforementioned models still exhibit two important shortcomings. First, most models (e.g. Refs. [13,15–18]) only consider symmetric laminates as this simplifies the calculations by setting matrix B equal to zero in CLT (see Section 2.3). However, this assumption is unrealistic for Type IV pressure vessels, which often involve asymmetric lay-ups. As shown by Camilleri et al. [17], using CLT with symmetry assumptions for asymmetric lay-ups can result in errors up to 33%. Note that only the analytical model by Jiang et al. [11] is valid for asymmetric lay-ups, but was solved numerically since closed-form equations could not be obtained. Secondly, CLT assumes a state of plane stress, thereby neglecting any contribution from out-of-plane stresses [15]. While this assumption may be adequate for thin-walled cylinders with a thickness-over-radius ratio below 1/10, Type IV pressure vessels for hydrogen storage are thick-walled, with composite thicknesses easily up to 30 mm due to the high working pressure. This means that a thin-walled assumption is not valid for this case and that out-of-plane stresses must be included in the analysis to obtain accurate results [17,19].

The second category is based on *3D elasticity theory* which assumes a 3D stress state. In the literature, there are two primary methods for deriving the 3D stress, strain, and displacement expressions: either according to Lekhnitskii [20], as followed by Wild and Vickers [14], Parnas and Katirci [19], and Tabakov and Summers [21], or alternatively according to Herakovich [22], as followed by Xia et al. [23], Bakaiyan et al. [24], Aimmanee [25] and Soleimani et al. [26]. Since out-of-plane stresses are incorporated, 3D elasticity theory is thought to yield more accurate predictions for thick-walled multilayered tubes compared to CLT [17,19]. Another advantage is that multiple input loads can be combined, typically including the internal pressure P_i, external pressure P_o, axial force F_x and torque T_x. It is even possible to include temperature variations ΔT to capture residual stresses [22,24,26]. Moreover, there are no limitations regarding the symmetry of the lay-up. Nonetheless, the biggest disadvantage of applying 3D elasticity theory to pressure vessels is that it cannot predict the cylinder edge effects. Indeed, it assumes a long tube for which the solution is only valid far from the edges [22]. Considering the importance of the dome-cylinder transition effects in pressure vessels, this assumption poses a serious limitation on the model's predictive capability in this region.

This literature review reveals that even the most advanced existing models have limitations in accurately predicting the response of thick-walled hydrogen pressure vessels. The objective of our research was to overcome this gap in the literature by developing a novel analytical model for the cylinder region of Type IV composite pressure with three features that are essential for a correct analysis; our model is (1) valid for asymmetric lay-ups, (2) includes out-of-plane stresses, and (3) can predict the cylinder edge effects. Moreover, we aimed to derive closed-form analytical equations that require no iterative methods or numerical approximations, in order to minimize the computational time.

The key to developing our analytical model was the superposition of two models. Model 1 is based on 3D elasticity theory, following the approach by Herakovich [22], and calculates the general response of a cylinder subjected to internal pressure P_i, external pressure P_o, axial force F_x, and torque T_x. Model 2 is based on CLT and predicts the local response of a cylinder subjected to an edge bending moment M_x^0 and shear force Q_x^0. It is an extension of the work by Belardi et al. [18] from symmetric to asymmetric lay-ups, and fits within the framework of bending theory for cylindrical shells. Although Model 2 assumes a plane stress state, it will be shown that this assumption is sufficient when used to predict edge effects only. In conclusion, our analytical model adopts a smart combination of the accuracy of 3D elasticity theory and the ability of CLT models to capture the edge effects, while bypassing their respective weaknesses.

2. Theory

This section presents the analytical derivations for Model 1 and 2, including their superposition method.

2.1. Definition of the coordinate systems and input parameters

First, a global cylindrical right-handed coordinate system (x, θ, r) is defined for Model 1, where x represents the axial direction, θ the circumferential direction, and r the radial direction, as illustrated in Fig. 2. Model 2 requires a modified right-handed cylindrical coordinate system (x, θ, z), where the origin is located at the midplane of the laminate and the z-axis is oriented inwards. Note that $z = r - R$ with R the radius of the midplane. The local material coordinate system $(1,2,3)$ is also right-handed and is defined for each layer k with a winding angle α_k relative to the x-axis, with 1 parallel to the fiber, 2 transverse to the fiber in-plane and 3 transverse to the fiber out-of-plane.

The required dimensions of the composite laminate are the inner radius R_i, the outer radius R_o, the thickness t and the half-length $L/2$, considering symmetry about the center. The laminate consists of N layers, numbered outwards ($k = 1, \ldots N$), which are assumed to be

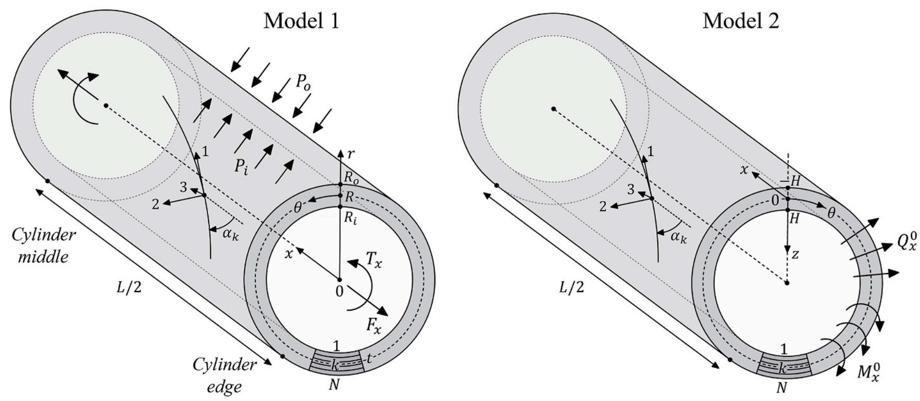

Fig. 2. Required coordinate systems, dimensions, lay-up, and loads for Model 1 and Model 2.

perfectly bonded. The composite material is modeled with linear elastic, orthotropic behavior, though the model is also applicable to (transversally) isotropic materials. The polymer liner is assumed to be not load-bearing, making our model applicable to Type V vessels as well. Additionally, small deformations are assumed for the kinematic relations. These assumptions suggest that the model should be used with caution when analyzing vessels nearing failure, particularly when large strains or delamination are present.

The lay-up can be either symmetric or asymmetric, but should consist solely of hoop layers with an angle of exactly 90°, and helical layers defined by a repetition of a balanced and symmetric lay-up: $[+\alpha_k, -\alpha_k, -\alpha_k, +\alpha_k]_n$. For $n \to \infty$, this resembles the real structure of filament wound helical layers, which consist of equal portions of intertwined tows with a positive and negative winding angle. Note that it is sufficient to choose $n \geq 2$ in practice.

The loads include a uniform internal pressure P_i, typically the working pressure, and an external pressure P_o which is usually negligible. In addition, an axial force F_x is required to establish the axial equilibrium with the dome. This is accomplished by defining F_x as the resultant of the pressure in the section plane with the dome, given by equation (1).

$$F_x = \pi R_i^2 P_i \tag{1}$$

Next, the axial torque T_x should be zero, considering that neither the hoop nor the helically intertwined layers induce axial twisting of the composite tube. Model 1 (Section 2.2) examines the overall deformation of a cylinder subjected to these four loads, without considering the edge effects.

Lastly, connecting the cylinder to the dome also requires that the displacement field of both components match at the junction. As a result, the actual displacement field near the cylinder edge deviates from the predictions made by Model 1. Model 2 (Section 2.3) addresses these local bending effects by considering an axisymmetric shear force Q_x^0 and bending moment M_x^0 at the cylinder edge ($x = 0$), both defined as positive outwards.

2.2. Model 1: 3D elasticity theory for the general response to $\boldsymbol{P_i}, \boldsymbol{P_o}, \boldsymbol{F_x}$ and $\boldsymbol{T_x}$

Model 1 considers a thick-walled multilayered cylinder subjected to P_i, P_o, F_x and T_x.

With u the axial displacement, v the circumferential displacement, and w the radial displacement, we can define the 3D **strain-displacement equations** in cylindrical (x, θ, r) coordinates [27].

$$\varepsilon_x = \frac{\partial u}{\partial x}, \varepsilon_\theta = \frac{1}{r}\left(\frac{\partial v}{\partial \theta} + w\right), \varepsilon_r = \frac{\partial w}{\partial r}$$

$$\gamma_{\theta r} = \frac{1}{r}\left(\frac{\partial w}{\partial \theta} - v + r\frac{\partial v}{\partial r}\right), \gamma_{xr} = \frac{\partial u}{\partial r} + \frac{\partial w}{\partial x}, \gamma_{\theta x} = \frac{\partial v}{\partial x} + \frac{1}{r}\frac{\partial u}{\partial \theta} \tag{2}$$

The 3D **constitutive equations** in global cylindrical coordinates are given by equation (3) where $[\overline{C}]_k$ is the transformed stiffness matrix for an orthotropic layer k with fiber angle α_k, defined according to formula (4). For the definition of the transformation matrices $[T_1]$ and $[T_2]$ and the stiffness matrix $[C]$, the reader is referred to Ref. [22].

$$\begin{bmatrix} \sigma_x \\ \sigma_\theta \\ \sigma_r \\ \tau_{\theta r} \\ \tau_{xr} \\ \tau_{x\theta} \end{bmatrix} = \begin{bmatrix} \overline{C_{11}} & \overline{C_{12}} & \overline{C_{13}} & 0 & 0 & \overline{C_{16}} \\ \overline{C_{12}} & \overline{C_{22}} & \overline{C_{23}} & 0 & 0 & \overline{C_{26}} \\ \overline{C_{13}} & \overline{C_{23}} & \overline{C_{33}} & 0 & 0 & \overline{C_{36}} \\ 0 & 0 & 0 & \overline{C_{44}} & \overline{C_{45}} & 0 \\ 0 & 0 & 0 & \overline{C_{45}} & \overline{C_{55}} & 0 \\ \overline{C_{16}} & \overline{C_{26}} & \overline{C_{36}} & 0 & 0 & \overline{C_{66}} \end{bmatrix} \begin{bmatrix} \varepsilon_x \\ \varepsilon_\theta \\ \varepsilon_r \\ \gamma_{\theta r} \\ \gamma_{xr} \\ \gamma_{x\theta} \end{bmatrix} \tag{3}$$

$$[\overline{C}]_k = [T_1(-\alpha_k)][C][T_2(\alpha_k)] \tag{4}$$

The 3D **equilibrium equations** in cylindrical coordinates are given by equations (5 – 7) [22].

$$\frac{\partial \sigma_r}{\partial r} + \frac{1}{r}(\sigma_r - \sigma_\theta) + \frac{1}{r}\frac{\partial \tau_{\theta r}}{\partial \theta} + \frac{\partial \tau_{xr}}{\partial x} = 0 \tag{5}$$

$$\frac{\partial \tau_{\theta r}}{\partial r} + \frac{1}{r}\frac{\partial \sigma_\theta}{\partial \theta} + \frac{\partial \tau_{x\theta}}{\partial x} + \frac{2}{r}\tau_{\theta r} = 0 \tag{6}$$

$$\frac{\partial \tau_{xr}}{\partial r} + \frac{1}{r}\frac{\partial \tau_{x\theta}}{\partial \theta} + \frac{\partial \sigma_x}{\partial x} + \frac{1}{r}\tau_{xr} = 0 \tag{7}$$

The aforementioned equations can be simplified by assuming that the stresses, strains and displacements are independent from θ due to axisymmetric loading, and that the stresses, strains and radial displacement are also independent from x far from the edge where F_x and T_x are applied. The system of equations in (5 - 7) can then be solved according to Herakovich [22], leading to the closed-form expressions for the stresses and radial displacement per layer k as a function of r, displayed in (8 - 12).

$$\sigma_{x,k}(r)=\left(\overline{C}_{11,k}+\left(\overline{C}_{13,k}+\overline{C}_{12,k}\right)\Gamma_{\mathrm{k}}\right)\varepsilon_x^0+\left(\left(\overline{C}_{12,k}+2\overline{C}_{13,k}\right)\Omega_{\mathrm{k}}+\overline{C}_{16,k}\right)\gamma^0 r+\left(\overline{C}_{12,k}+\lambda_k\overline{C}_{13,k}\right)A_{1,k}r^{\lambda_k-1}+\left(\overline{C}_{12,k}-\lambda_k\overline{C}_{13,k}\right)A_{2,k}r^{-\lambda_k-1} \tag{8}$$

$$\sigma_{\theta,k}(r)=\left(\overline{C}_{12,k}+\left(\overline{C}_{22,k}+\overline{C}_{23,k}\right)\Gamma_{\mathrm{k}}\right)\varepsilon_x^0+\left(\left(\overline{C}_{22,k}+2\overline{C}_{23,k}\right)\Omega_{\mathrm{k}}+\overline{C}_{26,k}\right)\gamma^0 r+\left(\overline{C}_{22,k}+\lambda_k\overline{C}_{23,k}\right)A_{1,k}r^{\lambda_k-1}+\left(\overline{C}_{22,k}-\lambda_k\overline{C}_{23,k}\right)A_{2,k}r^{-\lambda_k-1} \tag{9}$$

$$\tau_{x\theta,k}(r)=\left(\overline{C}_{16,k}+\left(\overline{C}_{26,k}+\overline{C}_{36,k}\right)\Gamma_{\mathrm{k}}\right)\varepsilon_x^0+\left(\overline{C}_{66,k}+\left(\overline{C}_{26,k}+2\overline{C}_{36,k}\right)\Omega_{\mathrm{k}}\right)\gamma^0 r+\left(\overline{C}_{26,k}+\lambda_k\overline{C}_{36,k}\right)A_{1,k}r^{\lambda_k-1}+\left(\overline{C}_{26,k}-\lambda_k\overline{C}_{36,k}\right)A_{2,k}r^{-\lambda_k-1} \tag{11}$$

$$w_k(r)=A_{1,k}r^{\lambda_k}+A_{2,k}r^{-\lambda_k}+\Gamma_{\mathrm{k}}\varepsilon_x^0 r+\Omega_{\mathrm{k}}\gamma^0 r^2 \tag{12}$$

$$\text{With } \Gamma_{\mathrm{k}}=\frac{\left(\overline{C}_{12,k}-\overline{C}_{13,k}\right)}{\left(\overline{C}_{33,k}-\overline{C}_{22,k}\right)},\Omega_{\mathrm{k}}=\frac{\left(\overline{C}_{26,k}-2\overline{C}_{36,k}\right)}{\left(4\overline{C}_{33,k}-\overline{C}_{22,k}\right)} \text{ and } \lambda_k=\sqrt{\frac{\overline{C}_{22,k}}{\overline{C}_{33,k}}} \tag{13}$$

Note that the stresses in local coordinates can easily be obtained by using the transformation matrix $[T_1]$. Moreover, the full derivation by Herakovich [22] reveals that the transverse shear stresses $\tau_{\theta r}$ and τ_{xr} are zero for the considered loads, and that the axial strain ε_x^0 and the angle of twist per unit of length γ^0 are constant throughout all the layers.

For a tube with N layers, there are still $2N+2$ unknowns in expressions (8 - 12), i.e. $\varepsilon_x^0, \gamma^0, A_{1,k}$ and $A_{2,k}$, which are found by a system of $2N+2$ equations. These include the 2 boundary conditions in (14), the $2(N-1)$ continuity equations in (15) by assuming perfect bonding for $N-1$ interfaces, and the force and torque equilibrium in (16) and (17).

$$\textbf{Boundary conditions}: \sigma_{r,1}(R_i)=-P_i \text{ and } \sigma_{r,N}(R_o)=0 \tag{14}$$

$$\textbf{Continuity equations}: w_k=w_{k+1} \text{ and } \sigma_{r,k}=\sigma_{r,k+1} \text{ for interfaces } k=1,\dots N-1 \tag{15}$$

$$\textbf{Axial force equilibrium}: F_x=2\pi\sum_{k=1}^{N}\int_{r_{k-1}}^{r_k}\sigma_{x,k}(r)rdr=\pi R_i^2P_i \tag{16}$$

$$\textbf{Torque equilibrium}: T_x=2\pi\sum_{k=1}^{N}\int_{r_{k-1}}^{r_k}\tau_{x\theta,k}(r)r^2dr=0 \tag{17}$$

2.3. Model 2: Classical Laminate Theory for the edge response to Q_x^0 and M_x^0

Model 2 considers a multilayered cylinder subjected to an edge bending moment M_x^0 and an edge shear force Q_x^0 at $x=0$. The derivation of the closed-form formulas is an extension of the work by Belardi et al. [18] with two essential improvements. Firstly, Model 2 does not include the general response of a cylinder subjected to P_i and F_x since this was covered by Model 1, and since it is demonstrated later that this is not accurate with CLT for thick-walled cylinders. Secondly, the derivations are extended to asymmetric lay-ups, meaning that matrix B in formula (19) is not necessarily zero. Note that matrices A, B and D in (18 - 20) represent the extensional stiffness, the bending-extension coupling stiffness, and the bending stiffness respectively, with $i,j\in\{1,2,6\}$ and $[\overline{Q}]_k$ the transformed reduced stiffness matrix [22].

$$A_{ij}=\sum_{k=1}^{N}\overline{Q_{ij}^k}(z_k-z_{k-1}) \tag{18}$$

$$B_{ij}=\frac{1}{2}\sum_{k=1}^{N}\overline{Q_{ij}^k}(z_k^2-z_{k-1}^2) \tag{19}$$

$$D_{ij}=\frac{1}{3}\sum_{k=1}^{N}\overline{Q_{ij}^k}(z_k^3-z_{k-1}^3) \tag{20}$$

It can be found that for lay-ups comprising only hoop layers with $\alpha_k=90^\circ$, and helical layers with $[+\alpha_k,-\alpha_k,-\alpha_k,+\alpha_k]_n$, $A_{16}=A_{26}=B_{16}=B_{26}=0$ and $D_{16},D_{26}\to 0$ as $n\to\infty$. This is demonstrated in Table 1 for an arbitrary asymmetric lay-up with one helical and one hoop layer of 1 mm for both $n=2$ and 5, and by using the elastic constants in Table 3. Additionally, for this asymmetric lay-up B_{11}, B_{12} and B_{22} are clearly different from zero, which emphasizes the significance of including these in our model.

Formula (21) presents the **strain-displacement equations** in cylindrical (x,θ,z) coordinates for the strain and curvature changes of the midplane [18].

$$\begin{bmatrix}\varepsilon_x^0\\ \varepsilon_\theta^0\\ \gamma_{x\theta}^0\\ \kappa_x\\ \kappa_\theta\\ \kappa_{x\theta}\end{bmatrix}=\begin{bmatrix}\dfrac{\partial u}{\partial x}\\ \dfrac{1}{R}\dfrac{\partial v}{\partial\theta}-\dfrac{w}{R}\\ \dfrac{1}{R}\dfrac{\partial u}{\partial\theta}+\dfrac{\partial v}{\partial x}\\ -\dfrac{\partial^2 w}{\partial x^2}\\ -\dfrac{1}{R^2}\left(\dfrac{\partial v}{\partial\theta}+\dfrac{\partial^2 w}{\partial\theta^2}\right)\\ -\dfrac{1}{R}\left(\dfrac{\partial v}{\partial x}+\dfrac{\partial^2 w}{\partial x\partial\theta}\right)\end{bmatrix} \tag{21}$$

These equations can be simplified by assuming that the tangential displacement v and the derivatives with respect to θ are zero. This assumption is generally true for the axisymmetric loading of isotropic shells of revolution [28], but can be extended to orthotropic materials if specific laminates are considered [18], including our lay-up which contains only hoop layers of 90° and helical layers with $[+\alpha_k,-\alpha_k,-\alpha_k,+\alpha_k]_n$.

Table 1
Components of ABD matrix for a lay-up $\left[[+30^\circ,-30^\circ,-30^\circ,+30^\circ]_n,90^\circ\right]$ with $n=2$ and 5.

	A_{16}	A_{26}	B_{11}	B_{12}	B_{22}	B_{16}	B_{26}	D_{16}	D_{26}
$n=2$	0.0	0.0	4.0e4	1.2e4	−6.3e4	0.0	0.0	6.8e-1	2.6e-1
$n=5$	0.0	0.0	4.0e4	1.2e4	−6.3e4	0.0	0.0	1.1e-1	4.1e-2

$$\begin{bmatrix} \varepsilon_x^0 \\ \varepsilon_\theta^0 \\ \gamma_{x\theta}^0 \\ \kappa_x \\ \kappa_\theta \\ \kappa_{x\theta} \end{bmatrix} = \begin{bmatrix} \dfrac{du}{dx} \\ -\dfrac{w}{R} \\ 0 \\ -\dfrac{d^2w}{dx^2} \\ 0 \\ 0 \end{bmatrix} \tag{22}$$

The **constitutive equations** for plane stresses in cylindrical coordinates are defined in formula (23) [18,22].

$$\begin{bmatrix} \sigma_x \\ \sigma_\theta \\ \tau_{x\theta} \end{bmatrix}_k = [\overline{Q}]_k \left(\begin{bmatrix} \varepsilon_x^0 \\ \varepsilon_\theta^0 \\ \gamma_{x\theta}^0 \end{bmatrix} + z \begin{bmatrix} \kappa_x \\ \kappa_\theta \\ \kappa_{x\theta} \end{bmatrix} \right) \tag{23}$$

Next, the three **equilibrium equations** in (24 - 26) must be considered [18].

$$\frac{dN_x}{dx} = 0 \tag{24}$$

$$\frac{dQ_x}{dx} + \frac{N_\theta}{R} = 0 \tag{25}$$

$$\frac{dM_x}{dx} - Q_x = 0 \tag{26}$$

Lastly, formulas (27 - 28) present the stress resultants and bending moments in which all the 16 and 26 terms are zero.

$$\begin{bmatrix} N_x \\ N_\theta \\ N_{x\theta} \end{bmatrix} = \begin{bmatrix} A_{11} & A_{12} & 0 \\ A_{12} & A_{22} & 0 \\ 0 & 0 & A_{66} \end{bmatrix} \begin{bmatrix} \varepsilon_x^0 \\ \varepsilon_\theta^0 \\ \gamma_{x\theta}^0 \end{bmatrix} + \begin{bmatrix} B_{11} & B_{12} & 0 \\ B_{12} & B_{22} & 0 \\ 0 & 0 & B_{66} \end{bmatrix} \begin{bmatrix} \kappa_x \\ \kappa_\theta \\ \kappa_{x\theta} \end{bmatrix} \tag{27}$$

$$\begin{bmatrix} M_x \\ M_\theta \\ M_{x\theta} \end{bmatrix} = \begin{bmatrix} B_{11} & B_{12} & 0 \\ B_{12} & B_{22} & 0 \\ 0 & 0 & B_{66} \end{bmatrix} \begin{bmatrix} \varepsilon_x^0 \\ \varepsilon_\theta^0 \\ \gamma_{x\theta}^0 \end{bmatrix} + \begin{bmatrix} D_{11} & D_{12} & 0 \\ D_{12} & D_{22} & 0 \\ 0 & 0 & D_{66} \end{bmatrix} \begin{bmatrix} \kappa_x \\ \kappa_\theta \\ \kappa_{x\theta} \end{bmatrix} \tag{28}$$

By inserting the strain-displacement equations (22) into (27 - 28), we find expressions (29 - 31).

$$N_x = A_{11}\frac{du}{dx} - A_{12}\frac{w}{R} - B_{11}\frac{d^2w}{dx^2} \tag{29}$$

$$N_\theta = A_{12}\frac{du}{dx} - A_{22}\frac{w}{R} - B_{12}\frac{d^2w}{dx^2} \tag{30}$$

$$M_x = B_{11}\frac{du}{dx} - B_{12}\frac{w}{R} - D_{11}\frac{d^2w}{dx^2} \tag{31}$$

From (24), it follows that N_x is a constant, and by applying axial force equilibrium, we find that it is zero.

$$N_x = \frac{P_i R_i}{2} = 0 \tag{32}$$

By applying this to (29), we can derive expression (33) for $\frac{du}{dx}$.

$$\frac{du}{dx} = \frac{A_{12}}{A_{11}}\frac{w}{R} + \frac{B_{11}}{A_{11}}\frac{d^2w}{dx^2} \tag{33}$$

Furthermore, by combining (25) and (26), we find equation (34).

$$\frac{d^2M_x}{dx^2} + \frac{N_\theta}{R} = 0 \tag{34}$$

By substituting (33) into (30), we find expression (35) for N_θ which is only a function of $w(x)$.

$$N_\theta = \left(\frac{A_{12}B_{11}}{A_{11}} - B_{12} \right) \frac{d^2w}{dx^2} + \left(\frac{A_{12}^2}{A_{11}} - A_{22} \right) \frac{w}{R} \tag{35}$$

Next, by taking the second derivative of M_x in (31), and by replacing $\frac{d^3u}{dx^3}$ with the second derivative of $\frac{du}{dx}$ in (33), we find formula (36) for $\frac{d^2M_x}{dx^2}$ as a function of $w(x)$.

$$\frac{d^2M_x}{dx^2} = \left(\frac{B_{11}^2}{A_{11}} - D_{11} \right) \frac{d^4w}{dx^4} + \frac{1}{R}\left(\frac{A_{12}B_{11}}{A_{11}} - B_{12} \right) \frac{d^2w}{dx^2} \tag{36}$$

Finally, by inserting (35) and (36) into (34), we obtain a fourth-order ordinary differential equation (37), which can be solved for $w(x)$.

$$\left(\frac{B_{11}^2}{A_{11}} - D_{11} \right) \frac{d^4w}{dx^4} + \left(\frac{A_{12}B_{11}}{A_{11}} - B_{12} \right) \frac{2}{R}\frac{d^2w}{dx^2} + \left(\frac{A_{12}^2}{A_{11}} - A_{22} \right) \frac{w}{R^2} = 0 \tag{37}$$

The corresponding characteristic polynomial is provided in (38), for which we can find the 4 complex roots m_i given in (39).

$$\left(\frac{B_{11}^2}{A_{11}} - D_{11} \right) m^4 + \left(\frac{A_{12}B_{11}}{A_{11}} - B_{12} \right) \frac{2}{R} m^2 + \left(\frac{A_{12}^2}{A_{11}} - A_{22} \right) \frac{1}{R^2} = 0 \tag{38}$$

$$m_i = \frac{\left(\pm\sqrt{\sqrt{\left(D_{11}A_{11} - B_{11}^2\right)\left(A_{11}A_{22} - A_{12}^2\right)} + A_{12}B_{11} - B_{12}A_{11}} \pm i\sqrt{\sqrt{\left(D_{11}A_{11} - B_{11}^2\right)\left(A_{11}A_{22} - A_{12}^2\right)} - A_{12}B_{11} + B_{12}A_{11}} \right)}{\sqrt{2R\left(D_{11}A_{11} - B_{11}^2\right)}} \tag{39}$$

The solution to the differential equation can then be expressed according to formula (40).

$$w(x) = A_1 e^{m_1 x} + A_2 e^{m_2 x} + A_3 e^{m_3 x} + A_4 e^{m_4 x} \tag{40}$$

Keeping in mind the physical meaning of the solution, we expect a diminishing effect upon moving away from the edge [18]. Thus, only the roots m_i with a negative real part are included, yielding expression (41).

$$w(x) = e^{\frac{-\sqrt{\sqrt{\left(D_{11}A_{11} - B_{11}^2\right)\left(A_{11}A_{22} - A_{12}^2\right)} + A_{12}B_{11} - B_{12}A_{11}}}{\sqrt{2R\left(D_{11}A_{11} - B_{11}^2\right)}} x}$$

$$\bullet \left(A_1 e^{\frac{\sqrt{\sqrt{\left(D_{11}A_{11}-B_{11}^2\right)\left(A_{11}A_{22}-A_{12}^2\right)}-A_{12}B_{11}+B_{12}A_{11}}}{\sqrt{2R\left(D_{11}A_{11}-B_{11}^2\right)}}ix} + A_2 e^{\frac{-\sqrt{\sqrt{\left(D_{11}A_{11}-B_{11}^2\right)\left(A_{11}A_{22}-A_{12}^2\right)}-A_{12}B_{11}+B_{12}A_{11}}}{\sqrt{2R\left(D_{11}A_{11}-B_{11}^2\right)}}ix} \right) \tag{41}$$

Lastly, Euler's equation was used to remove the complex part of (41), resulting in the final expression (42) for $w(x)$ where β_1 and β_2 are two stiffness parameters, as formulated in (43 - 44).

$$w(x) = e^{-\beta_1 x}(C_1 \cos(\beta_2 x) + C_2 \sin(\beta_2 x)) \tag{42}$$

$$\beta_1 = \sqrt{\frac{\sqrt{\left(D_{11}A_{11} - B_{11}^2\right)\left(A_{11}A_{22} - A_{12}^2\right)} + A_{12}B_{11} - B_{12}A_{11}}{2R\left(D_{11}A_{11} - B_{11}^2\right)}} \tag{43}$$

$$\beta_2 = \sqrt{\frac{\sqrt{\left(D_{11}A_{11} - B_{11}^2\right)\left(A_{11}A_{22} - A_{12}^2\right)} - A_{12}B_{11} + B_{12}A_{11}}{2R\left(D_{11}A_{11} - B_{11}^2\right)}} \tag{44}$$

This solution is very similar to the complementary solution for $w(x)$ by Belardi et al. [18], but with the important difference that here two stiffness parameters are defined instead of one, and that these are also a function of B_{11}, B_{22} and B_{12}. One can verify that for $B_{11} = B_{22} = B_{12} = 0$ and $P_i = 0$, equal expressions are obtained to those by Belardi et al. [18].

The next step is to determine the unknown constants C_1 and C_2 by imposing the axisymmetric bending moment M_x^0 and shear force Q_x^0 per unit of circumference at the edge. Note that additional steps were taken to derive the expressions for $M_{x,x=0}$ and $Q_{x,x=0}$ in equations (45 - 46).

$$M_x^0 = M_{x,x=0} = \left(\frac{B_{11}A_{12}}{A_{11}} - B_{12}\right)\frac{C_1}{R} + \left(\frac{B_{11}^2}{A_{11}} - D_{11}\right)\left(\beta_1^2 C_1 - 2\beta_1\beta_2 C_2 - \beta_2^2 C_1\right) \tag{45}$$

$$Q_x^0 = Q_{x,x=0} = \left(\frac{B_{11}A_{12}}{A_{11}} - B_{12}\right)\frac{(\beta_2 C_2 - \beta_1 C_1)}{R} + \left(\frac{B_{11}^2}{A_{11}} - D_{11}\right)\left(- \beta_1^3 C_1 + 3\beta_1^2\beta_2 C_2 + 3\beta_1\beta_2^2 C_1 - \beta_2^3 C_2\right) \tag{46}$$

The system of two equations in (45 - 46) is then solved for the 2 unknowns C_1 and C_2, presented in (47 - 48).

$$C_1 = \frac{A_{11}R\left(\left(A_{12}B_{11} - A_{11}B_{12}\right)M_x^0 + R\left(- 2\beta_1 Q_x^0 + M_x^0\left(\beta_2^2 - 3\beta_1^2\right)\right)\left(A_{11}D_{11} - B_{11}^2\right)\right)}{\left(A_{11}B_{12} - A_{12}B_{11}\right)^2 + 2R\left(\beta_1^2 - \beta_2^2\right)\left(A_{11}B_{12} - A_{12}B_{11}\right)\left(A_{11}D_{11} - B_{11}^2\right) + R^2\left(\beta_1^2 + \beta_2^2\right)^2\left(A_{11}D_{11} - B_{11}^2\right)^2} \tag{47}$$

$$C_2 = \frac{A_{11}R\left(\left(A_{12}B_{11} - A_{11}B_{12}\right)\left(Q_x^0 + \beta_1 M_x^0\right) + R\left(Q_x^0\left(\beta_2^2 - \beta_1^2\right) + M_x^0\beta_1\left(3\beta_2^2 - \beta_1^2\right)\right)\left(A_{11}D_{11} - B_{11}^2\right)\right)}{\beta_2\left(\left(A_{11}B_{12} - A_{12}B_{11}\right)^2 + 2R\left(\beta_1^2 - \beta_2^2\right)\left(A_{11}B_{12} - A_{12}B_{11}\right)\left(A_{11}D_{11} - B_{11}^2\right) + R^2\left(\beta_1^2 + \beta_2^2\right)^2\left(A_{11}D_{11} - B_{11}^2\right)^2\right)} \tag{48}$$

Lastly, by using the strain-displacement equations in (22) and the solution for $w(x)$ in (42), we find the following closed-form expressions for ε_x^0, ε_θ^0 and κ_x.

$$\varepsilon_x^0 = \frac{du}{dx} = \frac{e^{-\beta_1 x}}{A_{11}}\left(\frac{A_{12}}{R}(C_1 \cos(\beta_2 x) + C_2 \sin(\beta_2 x)) + B_{11}\left(\cos(\beta_2 x)\left(\beta_1^2 C_1 - 2\beta_1\beta_2 C_2 - \beta_2^2 C_1\right) + \sin(\beta_2 x)\left(\beta_1^2 C_2 + 2\beta_1\beta_2 C_1 - \beta_2^2 C_2\right)\right)\right) \tag{49}$$

$$\varepsilon_\theta^0 = -\frac{w}{R} = -\frac{1}{R}e^{-\beta_1 x}(C_1 \cos(\beta_2 x) + C_2 \sin(\beta_2 x)) \tag{50}$$

$$\kappa_x = -\frac{d^2 w}{dx^2} = -e^{-\beta_1 x}\left(\cos(\beta_2 x)\left(\beta_1^2 C_1 - 2\beta_1\beta_2 C_2 - \beta_2^2 C_1\right) + \sin(\beta_2 x)\left(\beta_1^2 C_2 + 2\beta_1\beta_2 C_1 - \beta_2^2 C_2\right)\right) \tag{51}$$

The global stresses can then be obtained by equation (23) and the local stresses by transformation to fiber angle α_k. Finally, the expressions for the stress resultants and bending moments are given in Appendix A.

2.4. Combined model for $\boldsymbol{P_i}, \boldsymbol{P_o}, \boldsymbol{F_x}, \boldsymbol{T_x}, \boldsymbol{Q_x^0}$ and $\boldsymbol{M_x^0}$

Model 1 was derived for the general response of a multilayered tube subjected to P_i, P_o, F_x and T_x and yielded closed-form equations as a function of the radial coordinate, $f_1(r)$. Model 2 was derived for the edge response of a multilayered tube subjected to Q_x^0 and M_x^0 and yielded closed-form equations as a function of the axial coordinate, $f_2(x)$. By superposition of these two models, we obtain a combined model that predicts both the general and edge response for these six loads, with expressions that are a function of both x and r. The combined model can then be used to analyze the cylinder region of Type IV vessels subjected to $P_i, P_o = 0, F_x, T_x = 0, Q_x^0$ and M_x^0.

However, one additional step is needed to justify this superposition. Indeed, one should understand that the cylinder subjected to P_i and F_x in Model 1 also exhibits edge effects which were not yet included, given that Model 1 only generates the solution for these loads far from the edge. More specifically, the different values for the axial stress $\sigma_{x,k}(r)$ per layer k cause the free edge to bend under P_i and/or F_x. The bending moment associated with these additional edge effects can be calculated using equation (52) where $\sigma_{x,k}(r)$ is defined by formula (8) in Model 1, and $r - R = z$ is the distance to the laminate's midplane.

Table 2
Symmetric and asymmetric lay-up for the cylinder region of a typical Type IV pressure vessel.

Ply number	1	2	3	4	5	6	7	8	9	10	11	12	13	14	15	16	17	18	19	20
Symmetric (°)	**90**	15	75	**90**	20	65	**90**	10	**90**	35	35	**90**	10	**90**	65	20	**90**	75	15	**90**
Asymmetric (°)	**90**	15	15	**90**	20	10	**90**	10	70	**90**	35	35	**90**	60	**90**	75	75	**90**	25	**90**

Table 3
Elastic constants for a carbon fiber reinforced epoxy composite.

Elastic constants	E_1	E_2	E_3	ν_{12}	ν_{13}	ν_{23}	G_{12}	G_{13}	G_{23}
Value	147 GPa	10 GPa	10 GPa	0.27	0.27	0.35	7 GPa	7 GPa	3.7 GPa

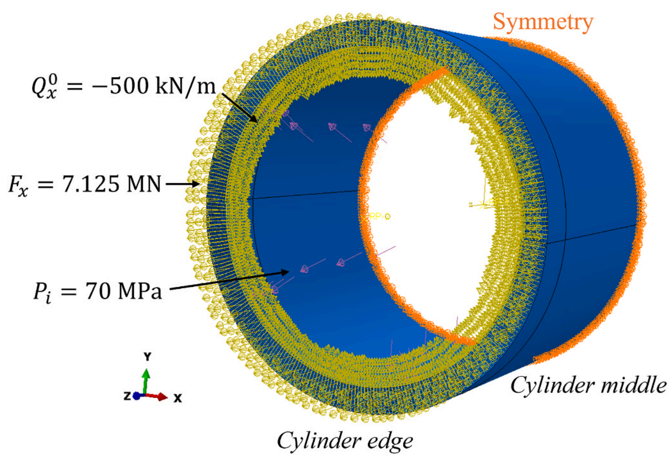

Fig. 3. Abaqus model of a cylinder subjected to P_i, F_x and Q_x^0 for numerical validation of our analytical model.

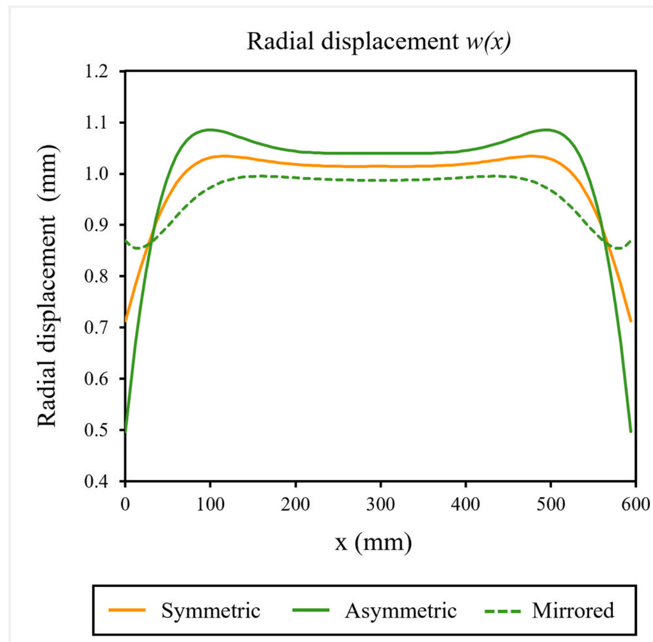

Fig. 4. Radial displacement as a function of x at $r = R_i$ for the three lay-ups and load case 2.

Table 4
β_1, β_2 and M_x^0 for the symmetric, asymmetric, and mirrored asymmetric lay-up.

	Symmetric lay-up	Asymmetric lay-up	Mirrored asymmetric lay-up
β_1 (m^{-1})	20.576	21.859	20.002
β_2 (m^{-1})	20.576	20.002	21.859
M_x^0 $\left(\frac{Nm}{m}\right)$	1254	−13623	15535

$$M_x^0 = \sum_{k=1}^{N} \int_{r_{k-1}}^{r_k} \sigma_{x,k}(r)(r-R)dr \tag{52}$$

Note that since the transverse shear stresses in Model 1 are zero, no additional edge shear force Q_x^0 is calculated to account for the extra edge effects. If the bending moment defined in (52) is then used as an additional input for M_x^0 in Model 2, the combined model incorporates all the edge effects. With this additional step, all the expressions for the stresses, strains and displacements in the combined model, $f_{comb}(x,r)$, can be calculated by superposition of Model 1 and 2, as illustrated by (53).

$$f_{comb}(x,r) = f_1(r) + f_2(x) \tag{53}$$

3. Materials and modelling methods

The combined analytical model is implemented as an efficient code in Python, with as input the dimensions, elastic constants, loads, and an array for the winding lay-up with corresponding layer thicknesses. The output comprises multiple 2D arrays for the displacements, strains and stresses, calculated at a chosen number of points in both the x- and r-direction. The elegance of the code is that extensions can easily be implemented, including rules of mixture for defining the elastic constants, or laminates composed of different materials.

For the analysis and verification of our analytical model in Section 4, we use a case study with realistic input parameters for the cylinder region of Type IV hydrogen pressure vessels. The cylinder has an inner radius R_i of 180 mm, a thickness t of 28.0 mm, and a half-length $L/2$ of 300 mm. It can be checked that t/R_i is indeed higher than 1/10, indicating that thick-walled theory is required. Both a symmetric and asymmetric lay-up are used for the analysis and are displayed in Table 2. These are based on realistic lay-ups, approximated by 20 layers with a fixed thickness of 1.4 mm and increments of 5° in winding angle. Both lay-ups consist of 40% hoop layers ($\alpha_k = 90°$), 20% high-angle helical layers ($\alpha_k > 45°$), and 40% low-angle helical layers ($\alpha_k < 45°$). A lay-up $[+\alpha_k/-\alpha_k/-\alpha_k/+\alpha_k]_2$ is used for each helical layer. The elastic constants in Table 3 are used, which are exemplary for a carbon fiber reinforced epoxy composite.

Furthermore, we consider two load cases. Load case 1 is defined by an inner pressure P_i of 70 MPa and an axial force F_x of 7.125 MN, calculated using formula (16). This first case is important to verify if the edge effects of a cylinder subjected to P_i and F_x in Model 1 are correctly predicted by formula (52). Load case 2 is equal to load case 1, but with an additional inward shear force Q_x^0 of - 500 kN/m at the edge. These are typical loads to which the cylinder region in a real pressure vessel is subjected.

Verification of our analytical model is performed by comparing to FE simulations in Abaqus. The Abaqus model shown in Fig. 3 was created by means of a solid extruded hollow cylinder, partitioned into 20 layers.

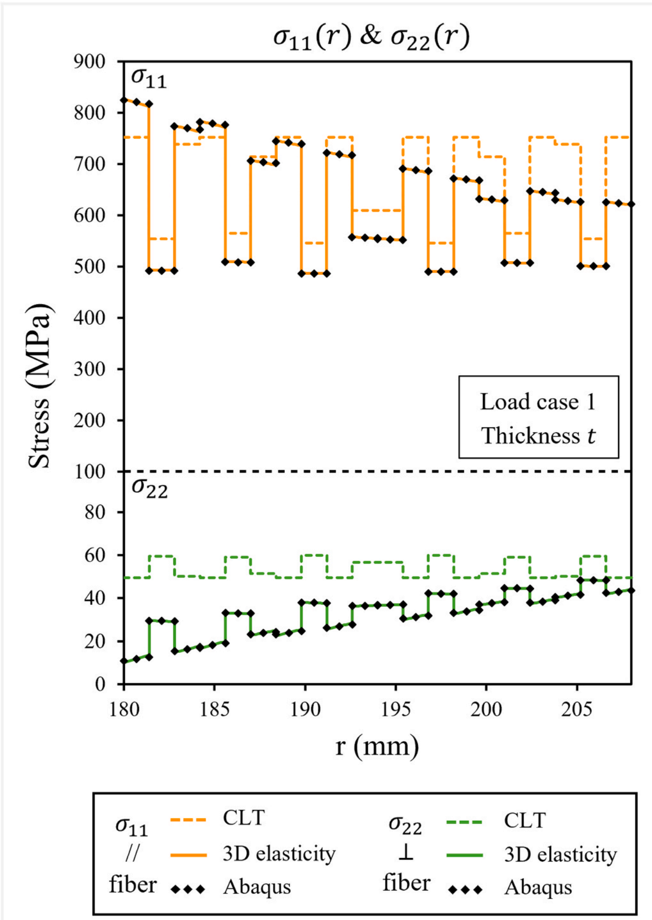

Fig. 5. σ_{11} and σ_{22} as a function of r at $x = L/2$ for symmetric lay-up and load case 1 by CLT, 3D elasticity theory, and Abaqus.

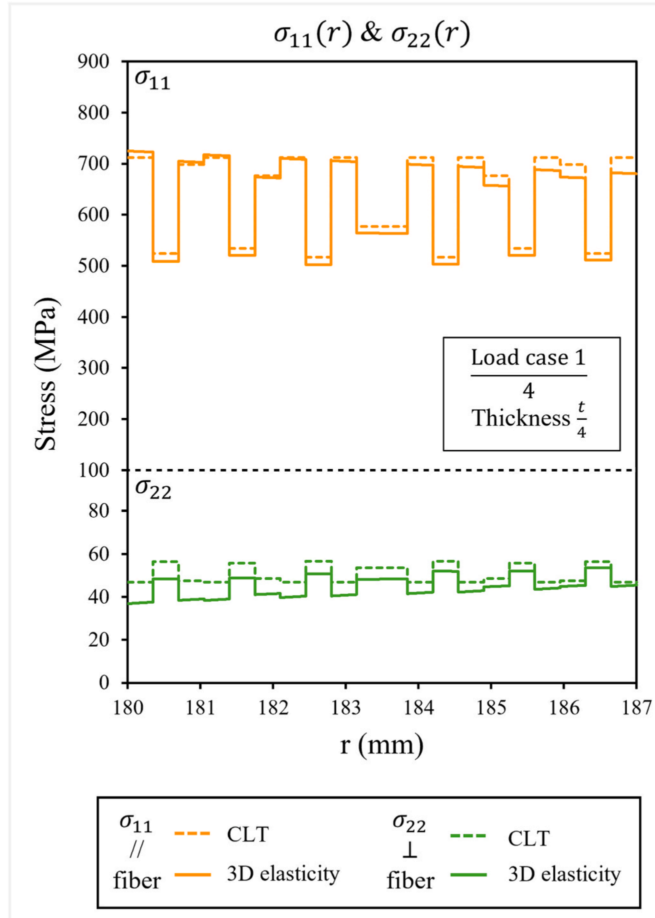

Fig. 6. σ_{11} and σ_{22} as a function of r at $x = L/2$ for symmetric lay-up with ¼ thickness and ¼ load case 1 by CLT and 3D elasticity theory.

A balanced and symmetric composite lay-up $[+\alpha_k/-\alpha_k/-\alpha_k/+\alpha_k]$ was assigned to each helical layer. A pressure of 70 MPa was applied to the inner surface. The edge surface representing the symmetry plane at the center was fixed for the axial and circumferential displacement in cylindrical coordinates, while the radial displacement was allowed. The edge surface representing the dome-cylinder transition had no displacement restrictions, but an axial force of 579 N/node and a shear force of - 49.6 N/node were applied to match the total contribution of all nodes to the values in load cases 1 and 2. The loads were assigned in separate steps to reproduce the different load cases. Finally, a structured mesh with additional refinement near the front edge was defined, consisting of 900,000 elements. Solid elements (C3D8R) were used to include out-of-plane stresses also for the numerical validation.

4. Results and discussion

4.1. Symmetric vs. asymmetric lay-ups

First, we study the values for β_1 and β_2 calculated by formulas (43 - 44) for both the symmetric and asymmetric lay-up. The results in Table 4 demonstrate that β_1 equals β_2 for the symmetric lay-up, which is expected since the formulas for β_1 and β_2 simplify to only one stiffness parameter for symmetric lay-ups, in agreement with the work by Belardi et al. [18]. In contrast, we obtain two different values for β_1 and β_2 for the asymmetric lay-up. Moreover, we mirrored the asymmetric lay-up, as shown in the last column, for which we can notice that β_1 and β_2 switch in value. This is due to the switching signs in $+A_{12}B_{11} - B_{12}A_{11}$ and $-A_{12}B_{11} + B_{12}A_{11}$ in the formulas for β_1 and β_2. This observation confirms that the two stiffness parameters in Model 2 allow us to distinguish between asymmetric lay-ups.

Table 4 also presents M_x^0, calculated using formula (52) for the three lay-ups and load case 1. This represents the bending moment associated with the bending of the free edge under the applied pressure and axial force. We detect the smallest value for M_x^0 for the symmetric lay-up, for which we indeed expect less bending. Besides, we notice that by mirroring the asymmetric lay-up, the sign of M_x^0 switches, which indicates that the bending direction of the free edge switches as well.

Fig. 4 displays the radial displacement for the three lay-ups and load case 2 as a function of x, mirrored at $x = L/2$, and at $r = R_i$. We observe that the negative value for Q_x^0 in load case 2 causes the free edge to bend inwards for all lay-ups. Nevertheless, the different values for β_1, β_2 and M_x^0 for the three lay-ups also influence the edge displacement. Particularly, the negative sign for M_x^0 for the asymmetric lay-up causes a further inward movement of the edge compared to the symmetric lay-up, whereas the positive sign for the mirrored lay-up opposes this inward movement. These results emphasize the importance of formula (52), where M_x^0 is clearly dependent on the lay-up.

4.2. Classical Laminate Theory vs. 3D elasticity theory

Next, we investigate our hypothesis that 3D elasticity theory is more accurate than CLT for Model 1, which handles the general response of thick-walled tubes. This was done by calculating the stresses for load case 1 and the symmetric lay-up using three methods: by CLT according to Belardi [18], by 3D elasticity theory according to Model 1, and by Abaqus. The local stresses (σ_{11} and σ_{22}) are plotted in Fig. 5 as a function

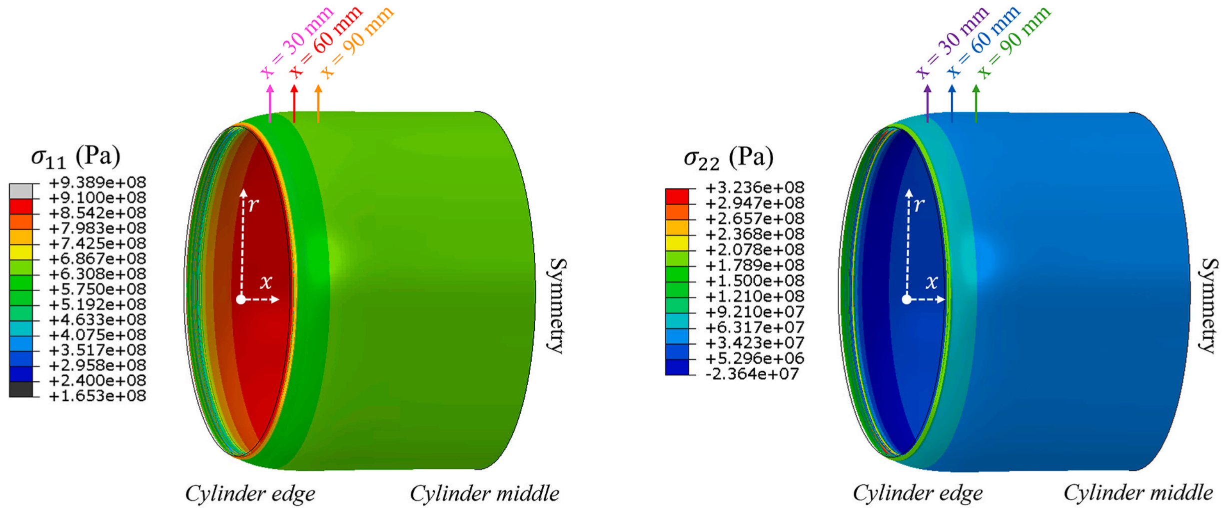

Fig. 7. σ_{11} and σ_{22} in Abaqus for asymmetric lay-up and load case 1 (deformation × 100).

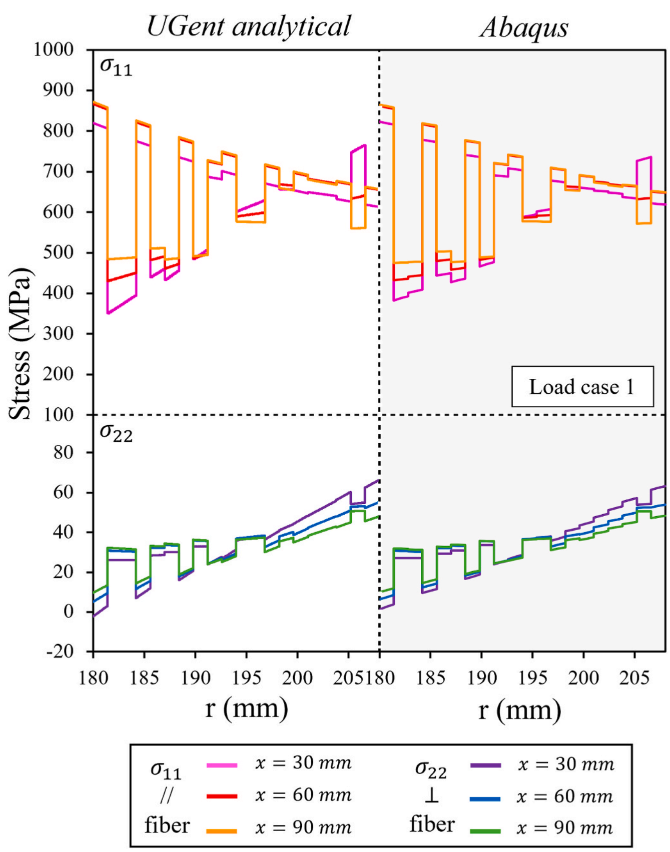

Fig. 8. σ_{11} and σ_{22} as a function of r at three x-positions for load case 1. Analytical model vs. Abaqus.

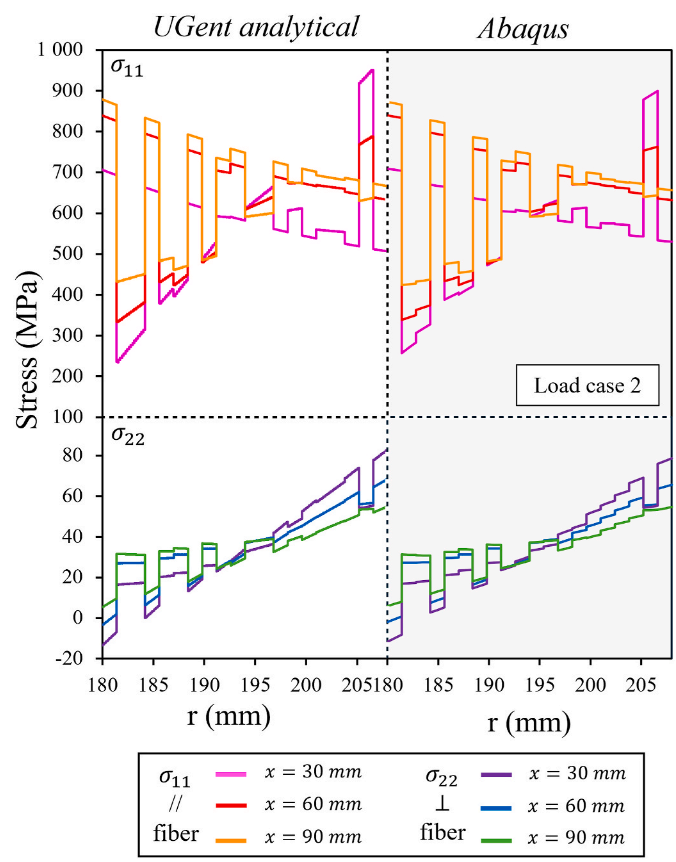

Fig. 9. σ_{11} and σ_{22} as a function of r at three x-positions for load case 2. Analytical model vs. Abaqus.

of r and at $x = L/2$ to exclude any edge effects for this analysis. We observe significant mismatches between CLT and Abaqus, whereas 3D elasticity gives outstanding agreements. This is not surprising since $t/R_i = 28$ mm/180 mm $= 0.156$, which is too large for a thin-walled assumption (< 0.10). As an additional verification, this procedure was repeated for a vessel with $t/4$ such that $t/R_i = 0.0389 < 0.10$. Fig. 6 shows that 3D elasticity theory and CLT are now closer in agreement, but a slight mismatch remains. These observations indicate that as the tube's thickness increases, 3D elasticity theory becomes notably more accurate compared to CLT. Note that this finding highlights an important limitation of all the models based on CLT ([11,13,15–18]) when used for the analysis of thick-walled vessels for hydrogen storage.

4.3. *Numerical validation of proposed analytical model*

Lastly, we perform a thorough numerical validation of our analytical model by comparing the results to those obtained by Abaqus. We start by verifying if the edge effects for load case 1 and the asymmetric lay-up are correctly predicted by formula (52). A first qualitative check is made by analyzing the local stresses obtained by Abaqus displayed in Fig. 7. We

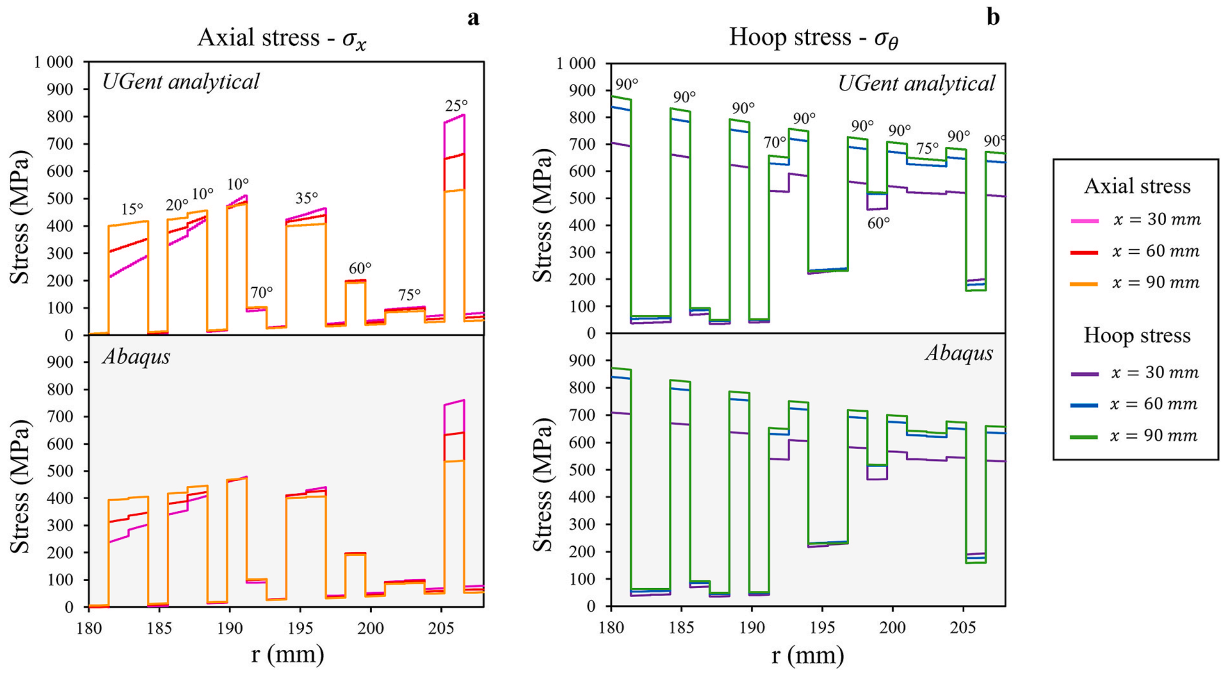

Fig. 10. σ_x (a) and σ_θ (b) as a function of r at three x-positions for load case 2, with indication of winding angles. Analytical model vs. Abaqus.

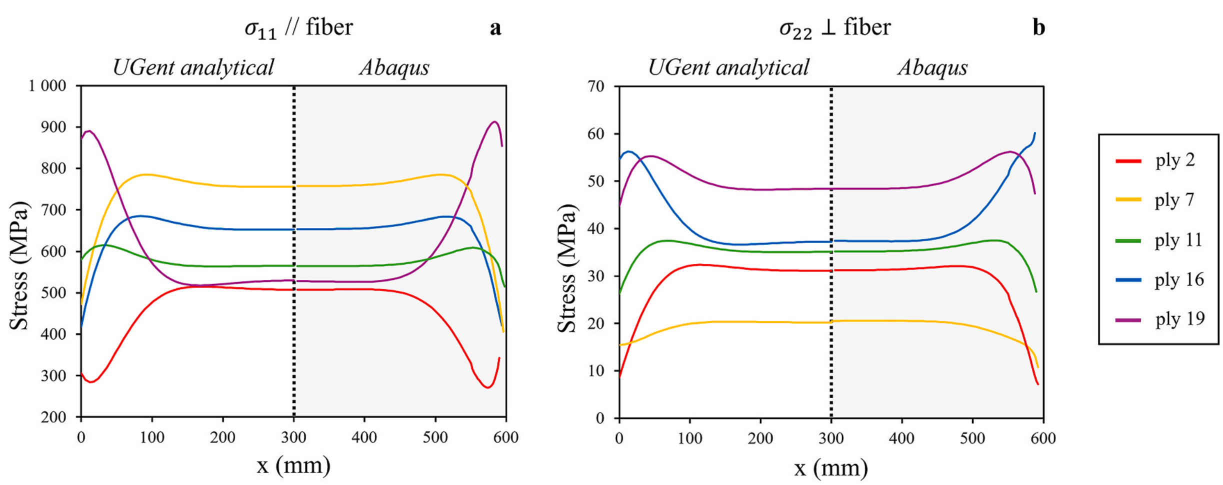

Fig. 11. σ_{11} (a) and σ_{22} (b) as a function of x for ply 2, 7, 11, 16 and 19 for load case 2. Analytical model vs. Abaqus.

observe that, despite Q_x^0 being zero for load case 1, the stresses clearly vary near the front edge, and that this edge is bent inwards as was predicted by the negative value for M_x^0 in Table 4 for the asymmetric lay-up

For quantitative verification, we plot the σ_{11} and σ_{22} stresses as a function of r at the three fixed x-positions indicated with arrows in Fig. 7. The results generated by our analytical model and Abaqus are compared in Fig. 8. We observe excellent agreements, both for the variations per ply (left to right), and for the variations at the three different x-positions (different colors), caused by the edge effects. This indicates a correct prediction of these edge effects, as well as a great overall accuracy. Moreover, this high accuracy was achieved with a Python script that runs in less than 1 second, while the Abaqus simulation has a runtime of 45 minutes with 8 CPUs. One should also not forget the time spent in Abaqus to create and analyze the model, in contrast to the ease of using a simple Python script.

Next, we study load case 2 for which Q_x^0 is added. The results for σ_{11} and σ_{22} are displayed in Fig. 9, which reveal that the additional shear force alters the stress state compared to Fig. 8, particularly near the edge at $x = 30$ mm. We again observe good agreements with Abaqus, confirming that the edge stresses caused by Q_x^0 are accurately predicted by our model.

The σ_{11} stresses in Fig. 9 can also be analyzed to assess the quality of the lay-up. An optimal design features a lay-up for which the hoop and helical plies are stressed equally for σ_{11}, such that there are no outliers which correspond to plies that fail more easily. However, we observe relatively large variations for σ_{11} with some outliers. If the design were optimized to reduce these variations, the overall composite thickness could be reduced, which could reduce weight and cost, and increase the inner volume to store hydrogen. Thanks to the very short calculation times of the Python code compared to Abaqus, an optimization algorithm can easily be combined with the analytical model to automate this optimization question.

Fig. 10 demonstrates that our model exhibits also strong agreements with Abaqus for the axial σ_x and hoop stresses σ_θ. Moreover, we can use these graphs to investigate the role of the hoop and helical layers in the

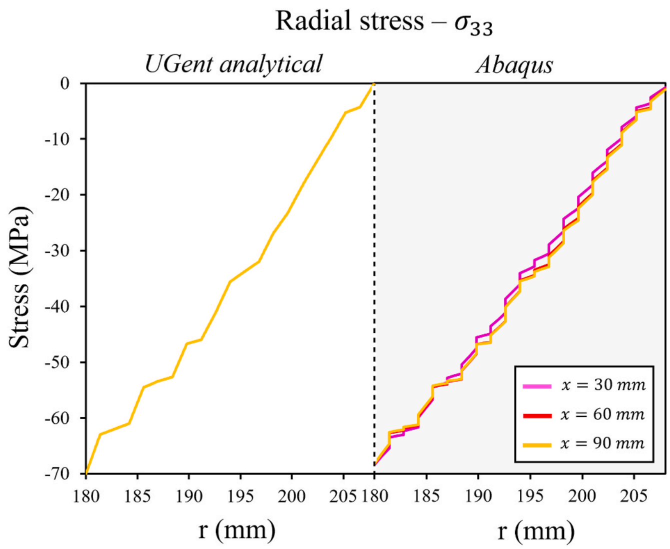

Fig. 12. σ_{33} as a function of r at three x-positions for load case 2. Analytical model vs. Abaqus.

cylindrical region of a pressure vessel. It can be observed that the low-angle helical layers take the largest stress in the axial direction, whereas the hoop layers take the largest stress in the hoop direction.

Next, the stresses are plotted as a function of x while keeping r constant. Fig. 11 shows the results for σ_{11} and σ_{22} for five plies (ply 2, 7, 11, 16 and 19). First, we observe that the graphs corresponding to the analytical model are very similar to those from Abaqus. The middle region displays relatively constant behavior which is predominantly predicted by the 3D elasticity theory in Model 1, while the edges show clear stress variations as a result of the superposition with Model 2. A second important observation is that the stresses near the edge can be significantly higher than those in the middle region. This highlights the importance of our analytical model which can predict these edge effects accurately.

Lastly, Fig. 12 displays the radial stresses (σ_{33}) as a function of r. This is purely a result of the 3D elasticity theory in Model 1, since Model 2 addresses only in-plane stresses. This is not a problem since significant edge variations are not expected for the radial stresses, considering that σ_{33} should always be in equilibrium with the internal P_i and outer pressure P_o at the inner and outer radius respectively, according to equation (14). This is supported by the Abaqus results in Fig. 12, which reveal almost no variations across different x-positions. Therefore, we can conclude that our model provides precise predictions for the radial stresses as well, which is a notable improvement over existing CLT models.

5. Conclusion

In this study, we presented a novel analytical model for predicting the stresses, strains, and displacements in the cylinder region of Type IV composite pressure vessels for hydrogen storage. Unlike any of the existing analytical models, our model combines three features of hydrogen pressure vessels that are crucial for a correct analysis. Firstly, our model is valid for asymmetric lay-ups, whereas many existing models are limited to symmetric lay-ups. Secondly, considering the thick composite overwrap required to store hydrogen at 70 MPa, 3D elasticity theory is used to account for out-of-plane stresses. Thirdly, our model effectively predicts the edge effects near the cylinder edge.

Our analytical model was developed by superimposing two models. Model 1 predicts the general response of a multilayered tube to internal and external pressures, axial force, and torque by 3D elasticity theory. Model 2 predicts the edge effects caused by an edge bending moment and shear force by Classical Laminate Theory, and is an extension of the work by Belardi et al. [18] to asymmetric layups.

Our model was shown to deliver valuable insights when it comes to analyzing asymmetric lay-ups. Additionally, verification with Abaqus confirmed that analytical models based on CLT, which address only in-plane stresses, exhibit significant errors when predicting the general response of thick-walled tubes. Lastly, multiple aspects of our model were verified by comparing the results to Abaqus. We observed excellent agreements for the stresses both as a function of the radial and axial coordinate, and for both the middle and edge region. In fact, these results were obtained in Python within 1 second thanks to the closed-form nature of the equations, in contrast to an Abaqus runtime of 45 minutes. Thanks to the unique combination of a high accuracy and computational speed, our analytical model is well-suited for parametric studies and design optimization algorithms. This could facilitate weight and cost reductions, as well as volume optimization of hydrogen pressure vessels, thereby enhancing their economic viability.

Funding

This work was supported by Research Foundation Flanders (FWO) [grant number 11P3A24N].

CRediT authorship contribution statement

Marie Hondekyn: Writing – original draft, Visualization, Validation, Software, Methodology, Investigation, Funding acquisition, Conceptualization. **Nazim Ali:** Writing – review & editing. **Wim Van Paepegem:** Writing – review & editing, Supervision, Project administration, Funding acquisition, Conceptualization.

Declaration of Generative AI and AI-assisted technologies in the writing process

During the preparation of this work the author used ChatGPT in order to improve the readability and intended message of specific paragraphs. After using this tool, the author reviewed and edited the content as needed and takes full responsibility for the content of the publication.

Declaration of competing interest

The authors declare that they have no known competing financial interests or personal relationships that could have appeared to influence the work reported in this paper

Acknowledgements

The author wishes to acknowledge Mohammad Hajikazemi for the insightful discussions during the performed research.

Appendix A. Expressions for stress resultants and bending moments derived in Model 2 (Section 2.3)

$$N_x(x) = 0 \tag{A.1}$$

$$N_\theta(x) = e^{-\beta_1 x}\left(\frac{1}{R}\left(\frac{A_{12}^2}{A_{11}} - A_{22}\right)(C_1\cos(\beta_2 x) + C_2\sin(\beta_2 x)) + \left(\frac{A_{12}B_{11}}{A_{11}} - B_{12}\right)\left(\cos(\beta_2 x)\left(\beta_1^2 C_1 - 2\beta_1\beta_2 C_2 - \beta_2^2 C_1\right) + \sin(\beta_2 x)\left(\beta_1^2 C_2 + 2\beta_1\beta_2 C_1 - \beta_2^2 C_2\right)\right)\right) \tag{A.2}$$

$$N_{x\theta}(x) = 0 \tag{A.3}$$

$$M_x(x) = e^{-\beta_1 x}\left(\frac{1}{R}\left(\frac{B_{11}A_{12}}{A_{11}} - B_{12}\right)(C_1\cos(\beta_2 x) + C_2\sin(\beta_2 x)) + \left(\frac{B_{11}^2}{A_{11}} - D_{11}\right)\left(\cos(\beta_2 x)\left(\beta_1^2 C_1 - 2\beta_1\beta_2 C_2 - \beta_2^2 C_1\right) + \sin(\beta_2 x)\left(\beta_1^2 C_2 + 2\beta_1\beta_2 C_1 - \beta_2^2 C_2\right)\right)\right) \tag{A.4}$$

$$M_\theta(x) = e^{-\beta_1 x}\left(\frac{1}{R}\left(\frac{B_{12}A_{12}}{A_{11}} - B_{22}\right)(C_1\cos(\beta_2 x) + C_2\sin(\beta_2 x)) + \left(\frac{B_{12}B_{11}}{A_{11}} - D_{12}\right)\left(\cos(\beta_2 x)\left(\beta_1^2 C_1 - 2\beta_1\beta_2 C_2 - \beta_2^2 C_1\right) + \sin(\beta_2 x)\left(\beta_1^2 C_2 + 2\beta_1\beta_2 C_1 - \beta_2^2 C_2\right)\right)\right) \tag{A.5}$$

$$M_{x\theta}(x) = 0 \tag{A.6}$$

References

[1] P. R. Shukla, J. Skea, and R. Slade, ‘Working Group III Contribution to the Sixth Assessment Report of the Intergovernmental Panel on Climate Change’.

[2] Alves MP, Gul W, Cimini Junior CA, Ha SK. A review on industrial perspectives and challenges on material, manufacturing, design and development of compressed hydrogen storage tanks for the transportation sector. Energies Jul. 2022;15(14):5152. https://doi.org/10.3390/en15145152.

[3] Staffell I, et al. The role of hydrogen and fuel cells in the global energy system. Energy Environ Sci 2019;12(2):463–91. https://doi.org/10.1039/C8EE01157E.

[4] Cullen DA, et al. New roads and challenges for fuel cells in heavy-duty transportation. Nat Energy May 2021;6(5):462–74. https://doi.org/10.1038/s41560-021-00775-z.

[5] Li M, et al. Review on the research of hydrogen storage system fast refueling in fuel cell vehicle. Int J Hydrogen Energy Apr. 2019;44(21):10677–93. https://doi.org/10.1016/j.ijhydene.2019.02.208.

[6] Roh HS, Hua TQ, Ahluwalia RK. Optimization of carbon fiber usage in Type 4 hydrogen storage tanks for fuel cell automobiles. Int J Hydrogen Energy Sep. 2013;38(29):12795–802. https://doi.org/10.1016/j.ijhydene.2013.07.016.

[7] Zhang Q, Xu H, Jia X, Zu L, Cheng S, Wang H. Design of a 70 MPa type IV hydrogen storage vessel using accurate modeling techniques for dome thickness prediction. Compos Struct Mar. 2020;236:111915. https://doi.org/10.1016/j.compstruct.2020.111915.

[8] Berro Ramirez JP, Halm D, Grandidier J-C, Villalonga S, Nony F. 700 bar type IV high pressure hydrogen storage vessel burst – simulation and experimental validation. Int J Hydrogen Energy Oct. 2015;40(38):13183–92. https://doi.org/10.1016/j.ijhydene.2015.05.126.

[9] Hua TQ, Roh H-S, Ahluwalia RK. Performance assessment of 700-bar compressed hydrogen storage for light duty fuel cell vehicles. Int J Hydrogen Energy Oct. 2017;42(40):25121–9. https://doi.org/10.1016/j.ijhydene.2017.08.123.

[10] Magneville B, Gentilleau B, Villalonga S, Nony F, Galiano H. Modeling, parameters identification and experimental validation of composite materials behavior law used in 700 bar type IV hydrogen high pressure storage vessel. Int J Hydrogen Energy Oct. 2015;40(38):13193–205. https://doi.org/10.1016/j.ijhydene.2015.06.121.

[11] Jiang W, Du F, Drechsler K, Zheng J. Combined composites layup architecture and mechanical evaluation of type IV pressure vessels: a novel analytical approach. Int J Hydrogen Energy May 2023;48(46):17565–76. https://doi.org/10.1016/j.ijhydene.2023.01.223.

[12] Leh D, Saffré P, Francescato P, Arrieux R, Villalonga S. A progressive failure analysis of a 700-bar type IV hydrogen composite pressure vessel. Int J Hydrogen Energy Oct. 2015;40(38):13206–14. https://doi.org/10.1016/j.ijhydene.2015.05.061.

[13] Park G, Kim C. Composite layer design using classical laminate theory for high pressure hydrogen vessel (type 4). Int J Precis Eng Manuf Apr. 2023;24(4):571–83. https://doi.org/10.1007/s12541-022-00752-w.

[14] Wild PM, Vickers GW. Analysis of filament-wound cylindrical shells under combined centrifugal, pressure and axial loading. Compos. Part Appl Sci Manuf Jan. 1997;28(1):47–55. https://doi.org/10.1016/S1359-835X(96)00093-0.

[15] Madhavi M. Design and analysis of filament wound composite pressure vessel with integrated-end domes. Defence Sci J Jan. 2009;59(1):73–81. https://doi.org/10.14429/dsj.59.1488.

[16] Alcántar V, Aceves SM, Ledesma E, Ledesma S, Aguilera E. Optimization of Type 4 composite pressure vessels using genetic algorithms and simulated annealing. Int J Hydrogen Energy Jun. 2017;42(24):15770–81. https://doi.org/10.1016/j.ijhydene.2017.03.032.

[17] Camilleri D, Ellul B, Muscat M. Design-by-Analysis methods for asymmetric or unbalanced cylindrical composite pressure vessels. In: Design and analysis, vol. 3. Anaheim, California, USA: American Society of Mechanical Engineers; Jul. 2014. https://doi.org/10.1115/PVP2014-28130. V003T03A011.

[18] Belardi VG, Ottaviano M, Vivio F. Bending theory of composite pressure vessels: a closed-form analytical approach. Compos Struct Feb. 2024;329:117799. https://doi.org/10.1016/j.compstruct.2023.117799.

[19] Parnas L, Katırcı N. Design of fiber-reinforced composite pressure vessels under various loading conditions. Compos Struct Oct. 2002;58(1):83–95. https://doi.org/10.1016/S0263-8223(02)00037-5.

[20] Lekhnitskii SG, Fern P, Brandstatter JJ, Dill EH. Theory of elasticity of an anisotropic elastic body. Phys Today Jan. 1964;17(1):84. https://doi.org/10.1063/1.3051394.

[21] Tabakov PY, Summers EB. Lay-up optimization of multilayered anisotropic cylinders based on a 3-D elasticity solution. Comput Struct Jan. 2006;84(5–6):374–84. https://doi.org/10.1016/j.compstruc.2005.09.023.

[22] Herakovich CT. Mechanics of fibrous composites. New York: Wiley; 1998.

[23] Xia M, Takayanagi H, Kemmochi K. Analysis of multi-layered filament-wound composite pipes under internal pressure. Compos Struct 2001.

[24] Bakaiyan H, Hosseini H, Ameri E. Analysis of multi-layered filament-wound composite pipes under combined internal pressure and thermomechanical loading with thermal variations. Compos Struct May 2009;88(4):532–41. https://doi.org/10.1016/j.compstruct.2008.05.017.

[25] Aimmanee S. A unified analysis of adhesive-bonded cylindrical coupler joints. In: Applied adhesive bonding in science and technology. IntechOpen; 2017. https://doi.org/10.5772/intechopen.72288.

[26] Soleimani M, Gholami R, Alijani A, Ansari R. An analytical solution for dynamics of cyclic thermomechanically loaded multi-layered filament-wound composite pipes in hygrothermal environment. Thin-Walled Struct Dec. 2023;193:111242. https://doi.org/10.1016/j.tws.2023.111242.

[27] Fung YC, Drucker DC. Foundation of solid mechanics. J Appl Mech Mar. 1966;33(1):238. https://doi.org/10.1115/1.3625018.

[28] Baker EH, Capelli AP, Kovalevsky L, Rish FL, Verette RM. Shell analysis manual. Technical Report. 1968. NASA-CR-912, NASA.